



CHALMERS
UNIVERSITY OF TECHNOLOGY



Loading and crushing of trapped ballast stones

Loading and deformation of a ballast stone trapped in a railway switch

Master's thesis in Applied Mechanics

ROBIN HAFSTRÖM

Department of Mechanics and Maritime Sciences
CHALMERS UNIVERSITY OF TECHNOLOGY
Gothenburg, Sweden 2020

MASTER'S THESIS 2020:61

Loading and crushing of trapped ballast stones

Loading and deformation of a ballast stone trapped in a railway
switch

ROBIN HAFSTRÖM



CHALMERS
UNIVERSITY OF TECHNOLOGY

Department of Mechanics and Maritime Sciences

Division of Dynamics

CHALMERS UNIVERSITY OF TECHNOLOGY

Gothenburg, Sweden 2020

Loading and crushing of trapped ballast stones
Loading and deformation of a ballast stone trapped in a railway switch
ROBIN HAFSTRÖM

© ROBIN HAFSTRÖM, 2020.

Supervisor: Björn Paulsson
Examiner: Anders Ekberg, Department of Mechanics and Maritime Sciences

Master's Thesis 2020:61
Department of Mechanics and Maritime Sciences
Division of Dynamics
Chalmers University of Technology
SE-412 96 Gothenburg
Telephone +46 31 772 1000

Cover: Picture of a ballast stone. Ballast stone provided by Björn Paulsson and photo taken by author.

Typeset in L^AT_EX
Printed by Chalmers Reproservice
Gothenburg, Sweden 2020

Loading and crushing of trapped ballast stones
Loading and deformation of a ballast stone trapped in a railway switch

ROBIN HAFSTRÖM

Department of Mechanics and Maritime Sciences
Chalmers University of Technology

Abstract

The Swedish railway reported 9000 faults in switches in 2017. One reason for these faults is the trapping of foreign objects in railway switches. However, a number of faults are also due to signaling where a sensor reports a false-positive error. One way to dispense of the problem with erroneous sensors are to remove them. This can only be done if safe operations can be obtained also without sensors. As a first investigation into this, the study will investigate the loading and deformation of ballast stones as well as assess when failure occurs during the switching operation.

The study can be divided into two parts: The first part is trying to find the largest stone that could get trapped in the switch when drivers are locking the switch rail. This was done by applying the combined load of two switch motors and a blocking stone in a numerical model and finding where the switch rail had the highest displacement. By testing different boundary conditions it was found that stones smaller than some 42 to 81 mm may get trapped under the assumptions in the simulations.

The second part of the study concerns the force required to reach failure in a ballast stone. Ballast stones of an approximate diameter of 40 mm are investigated. Both numerical simulations and tests were performed. The numerical model used a linear Drucker-Prager material model for the "plasticity" of the stone. The test of the ballast stones was performed using specialised stone crushing equipment. It was concluded that loads in the range of 15 to 60 kN are required to compress the ballast stone 20%. Numerical simulation results and test data did not fit well. This is due to the brittle fracture of the ballast stones not being sufficiently well captured in the numerical simulations.

Keywords: Railway, Switches, contact sensor, Drucker-Prager, Strength of granite, Ballast stone.

Acknowledgements

I am writing this as my work on this thesis draws to an end. I am happy for the people I have met and I am lucky for the opportunity I have gotten. It has been lots of work, hardships and small victories along the way. One thing I have learned during the writing of this thesis is to always be prepared for the surprises in life. In my case "life" was synonymous with "FE-sofware".

"Life is full of surprises, but never when you need one"
- Bill Watterson, "Homicidal Psycho Jungle Cat"

There are a number of people who helped make this work possible. First of, Magnus Evertsson, without whom I would not have been able to perform the crushing test, a key part of the thesis. Niklas Reck who helped maneuver the machine for the test and also kept me company during numerous lunch breaks. Anders Ahlquist at Vossloh who provided the invaluable CAD-model. I would also like to express my deepest gratitude to Björn Paulsson for his unending knowledge about the railway. Not only did his expertise provide a huge help but his positive spirits and can-do-attitude always brightened the day. Finally I would like to thank Anders Ekberg. His help and feedback have been invaluable. He has gone beyond and above with all the support he has given. No one could wish for a better examiner and teacher.

Robin Hafström, Gothenburg, August 2020

Contents

1	Introduction	1
1.1	Background	1
1.2	Aim	2
1.3	Methodology	2
1.4	Limitations	2
2	Theory	3
2.1	Railway switches	3
2.1.1	Motors and sensors	3
2.1.2	Ballast	4
2.2	Drucker-Prager	5
3	Methods	7
3.1	Crushing test of ballast stone	7
3.1.1	Ballast length and LT-index distribution	7
3.1.2	Crushing tests	8
3.1.3	Performing the crushing test	9
3.2	Estimation of maximum size of a ballast stone that may get trapped between switch and stock rail	10
3.2.1	Numerical model of a switch rail	10
3.2.2	Finite element analysis of the switch rail	12
3.2.3	Validation of the switch rail finite element analysis	13
3.3	Mechanical behaviour of trapped ballast stone	14
3.3.1	Model of ballast stone crushing	14
3.3.2	Stone geometries	14
3.3.3	Setting up the finite element analysis	16
4	Results	19
4.1	Results of ballast stone crushing tests	19
4.2	Results from finite element analyses	24
4.2.1	Bending of switch rail	24
4.2.2	Uniaxially loaded ballast stones	25
4.3	Validations of finite element analyses	29
4.3.1	Switch rail deformations	29
4.3.2	Stone crushing	30
4.3.3	Comparing FE simulations of stone crushing to test data	30

5 Discussion	33
5.1 Test data	33
5.2 Constitutive model	33
5.3 Simplifications and assumptions used in the switch blade deformation analysis	34
6 Conclusion	37
7 Further work	39
Bibliography	41
Computational Resources	43

1

Introduction

1.1 Background

The Swedish railway contains about 7 000 railway switches in main lines [1]. In 2017 there were close to 9 000 faults in switches reported to Trafikverket (The Swedish Transport Administration). These faults are more prominent during the harsh winter season, but occur all year round. [2]

One significant reason for faults are snow or ballast stones that get trapped and hinder the tongue to get in position. The tongue control contact (TKK) sensors are created just for this purpose: to make sure no objects are getting trapped. Without the TKK the fear is that a complete switching will occur while there being an object stuck in between the rails which could cause derailment. A complete switching means that the driving and locking devices have ensured sufficient switching at the positions of the driving devices. [2]

However the TKK sensors are not infallible. They sometimes give a warning of an object being stuck when there is none. Unwanted disruptions in the railway traffic are costly. [2] The simplest way to dispense of this problem would be to show that removing the TKKs poses no added risk of derailment. This study will not do that. However it will investigate the behaviour of trapped a ballast stone to support further studies towards this objective.



(a) Switching motors with the TKK marked in red. (b) The TKK.

Figure 1.1: Pictures of a switch. The two switching motors can be seen as well as the casing for the TKK. The switching mechanism at the switching motors have snow covers on them. The picture was taken at Vimmarnp operation site, track 1, switch 132b. Photo by J. Malm, Strukton Rail AB.

1.2 Aim

The aim of this thesis is to investigate the loading and deformation behaviour of a ballast stone trapped in a railway switch. Focus will be put on modeling the ballast stone and assess failure during switching operations.

1.3 Methodology

Two literature studies are conducted. One focuses on regulations and common standards regarding ballast according to Trafikverket (The Swedish Transport Administration). The second literature study is carried out to identify a suitable constitutive model for ballast. Time is also dedicated on learning the finite element software ABAQUS.

Two numerical simulations are carried out. The first simulation evaluates the load acting on a ballast stone when a complete switching has occurred. This simulation also estimates a largest stone length that still provides a complete switching provided switching motor limitations. The second simulation evaluates the stress and deformation in the ballast stone. The goal of this simulation is to assess ballast stone failures and find critical geometrical zones.

As a last step, before conclusions can be drawn, the two finite element models are validated. The first simulation, concerning the maximum force and size of the stone, will be validated by comparing to an analytic Euler–Bernoulli beam equation of a similar problem. The constitutive model and the second simulation will be compared with experimental data obtained from oedometric tests.

1.4 Limitations

The thesis was carried out at Chalmers University of Technology. Resources available at the university are primarily used. The project concerns one person and is limited to 30HP, corresponding to 20 study weeks.

As for the scope, the thesis will only consider a simplified model of one type of switch as well as one type of switching motor and only one of the two switching rails. Due to the previously mentioned time constraint the simulations will only consider static and quasi-static loads. This implies that the stone will be assumed fixed in position and will not slide sideways or upwards as might otherwise be the case. The loading from a passing train will not be considered.

2

Theory

2.1 Railway switches

The purpose of a switch is to guide trains from one track to another. This might be in junctions, where tracks converge or diverge. There are several different types of switches depending on the number of tracks as well as how the interaction of the tracks look. This study will be limited to a single railroad switch, the EV-60E-760-1:15. This switch has a curvature ratio of 1:15, a radii of 760 m and merge two tracks into a single track [3]. The choice of the EV-60E-760-1:15 switch is made because the switch is common and has a slim and long tongue. [4]

2.1.1 Motors and sensors

The railroad switch works by moving the switching rails laterally and leading the train to the desired track, see Figure 2.1. This lateral movement is achieved using the switching motors. When switching has occurred without errors, a clearing signal is given allowing trains to pass. In order to get a clearing signal both switch motors need to perform a full switch movement and there should not be any foreign objects in between the switch rail and the stock rail. If a sufficiently large foreign object is trapped, a contact control sensor (TKK) will raise an error. [5]

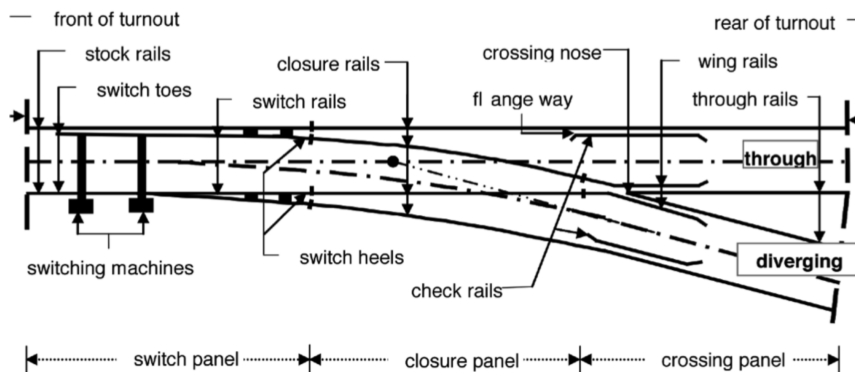


Figure 2.1: Illustration of a single railroad switch [6]

When performing the analysis it is assumed that the switch motor EasySwitch by Vossloh is used. This switch motor can produce a maximum force of 6.8 kN and has

a locking force of 100 kN [7].

2.1.2 Ballast

Ballast is an important and fundamental part of the railway. Its main purpose is to add stability and support to a rail structure. For ballast stones this concerns supporting the railway ties and rails and distributing loads. Ballast needs to be resistant to wear in order to withstand a high number of load cycles while maintaining its mechanical properties. It is also important for the ballast to have good draining properties as to not be affected by high rainfalls and freezing. [5]

In order to enforce a good quality of the ballast, Trafikverket (The Swedish Transport Administration) have guidelines in place for how ballast is to be produced and what mechanical and geometrical properties it shall have [8]. These guidelines are based on European standards. [9]

There are two classes of ballast in Sweden. The main difference is the particle size with Class I ballast being larger. Ballast of Class I shall have a particle size distribution in the range of 31.5 mm to 63 mm according to Figure 2.2. The second class of ballast is Class II with a size distribution of 11.2 mm to 31.5 mm. Both of these classes shall have a LT-index (length to width ratio) no larger than 3. [8]

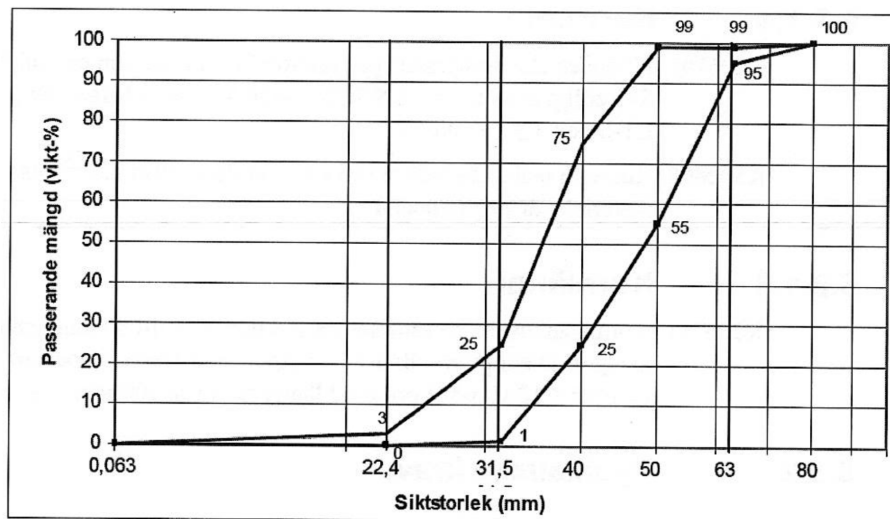


Figure 2.2: Ballast particle size according to SS-EN 13450, category E [9]. Figure from [8].

According to Trafikverket, stones used for ballast shall be of granite with a low content of mica. Gneiss and other hard and resistant rock types such as quartzite, diabase and porphyry may also be used [8] [10].

2.2 Drucker-Prager

The Drucker–Prager effective stress criterion, also known as the Extended von Mises criterion, is commonly used when predicting failures in geotechnical engineering [11]. In the finite element software ABAQUS Drucker-Prager models are used to model frictional materials such as rock and soils that undergo pressure-dependent yield [12].

The Drucker-Prager criterion is a generalization of the more commonly known Mohr-Coulomb criterion [13]. It may be expressed as

$$\alpha\sigma_m + \sqrt{J_2} + \kappa = 0 \quad (2.1)$$

where α and κ are material constants. J_2 is the second invariant of the stress deviator tensor defined as $J_2 = S_{ij}S_{ij}/2$ where S is linked to the stress tensor σ_{ij} as $S_{ij} = \sigma_{ij} - \sigma_m\delta_{ij}/3$. σ_m is the hydrostatic stress defined as $\sigma_m = \sigma_{ii}/3$. [11] And δ_{ij} is the Kronecker delta defined as $\delta_{ij} = 1$ when $i = j$ and $\delta_{ij} = 0$ when $i \neq j$. [14]

The advantage of the Drucker–Prager criterion is the simplicity in the sense that few material parameters are required. This makes it fairly easy to implement in numerical simulations. Drucker–Prager will give equal weight to the principal stresses. This tends to produce significant errors in triaxial stress states e.g. when $\sigma'_1 = \sigma'_2 < \sigma'_3$. The errors tend to over estimate the strength of the rock for general states of stress. By choosing material parameters to match the current load case, the results may be improved. The model also loses accuracy for tensile stresses. [13]

3

Methods

3.1 Crushing test of ballast stone

In the following section the methodology and sample selection from a crushing test is presented. The test sample was taken at Sävenäs from a smaller storage provided by Trafikverket. The sample was taken at random. The sample was then divided into two parts, one larger and one smaller. The large sample was employed to evaluate the distribution of the length of the stones as well as the ratio between the longest and the shortest sides of the stones (LT-index). The smaller sample is dedicated to be used in the crushing test and consists of 15 stones.

3.1.1 Ballast length and LT-index distribution

The large sample contains a total of 150 stones. The sample mostly consist of granite stones. In Figure 3.1 a bar graph of lengths and LT-indices is presented. In order to verify the normal distribution an Anderson-Darling test was performed using the MATLAB `adtest.m` function. The P-value for the length distribution was 0.39 and for the LT-indices it was 0.0005. With a significance level of 0.05 it is concluded that the LT-index distribution do not rejects the null-hypothesis regarding a normal distribution.

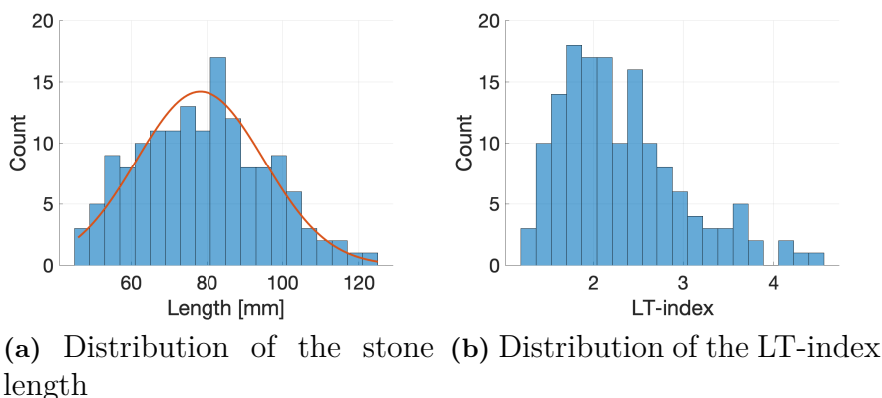


Figure 3.1: Size distributions of the large sample.

The length in this sample correspond to the longest side of the stones. The LT-index is the ratio between the longest and the shortest side of the stone. The average length of the sample is 78.7 mm with a standard deviation of 16.8 mm. The samples has

an LT-index median of 2.16. According to Trafikverket the LT-index shall be less than 3 [8].

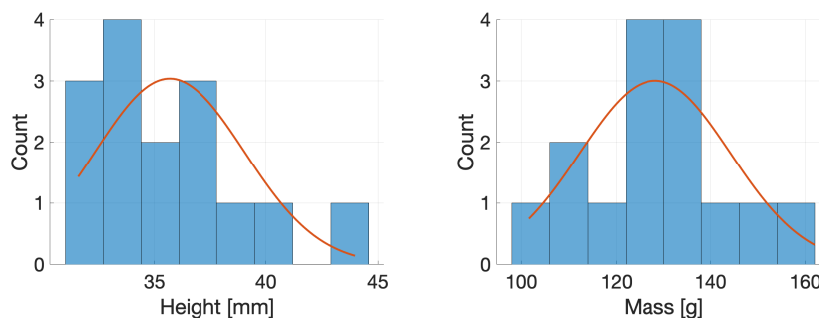
3.1.2 Crushing tests

Crushing tests were performed on 15 stones with an average diameter of 40 mm taken from the sample above. In Table 3.1 the height and the mass of the tested stones are presented. The loaded height refers to the height at which the stone was loaded. The average height of this sample is 35.7 mm. The average mass of the stones was 128 g with a standard deviation of 16 g. An Anderson-Darling test was performed using the MATLAB `adtest.m` function. P-values for the height and mass distributions were 0.24 and 0.86, respectively.

In Figure 3.2 the distribution curve for the loaded height and the mass of the small sample of stones to be crushed can be seen. These bar charts show more clearly that the majority of the stones are smaller than 40 mm and have a mass of around 130 g.

Table 3.1: The loaded length and mass of the small ballast stone sample used in the crushing test.

Stone no.	Height [mm]	Mass [g]	Stone no.	Height [mm]	Mass [g]
1	40.69	122.50	9	37.45	122.57
2	34.19	114.54	10	36.70	110.80
3	32.59	130.81	11	34.00	124.33
4	37.92	144.77	12	32.24	136.35
5	34.22	127.62	13	34.93	130.96
6	35.82	161.95	14	32.90	101.61
7	31.58	132.61	15	43.98	150.25
8	36.10	111.43			



(a) Distribution of the loaded height (b) Distribution of the mass

Figure 3.2: The distribution of the loaded height and the mass of the smaller test sample.

3.1.3 Performing the crushing test

The stone crushing test was performed using a hydraulic press. In Figure 3.3 the cross section of the test setup is sketched.

The procedure of the test for a single stone specimen was as follows: First, the weight and height of the stone were recorded. The stone was then placed in the cylindrical tool, Figure 3.3. The machine then compressed the stone until a 20% reduction of the initial height was achieved. The feeding rate was 5 mm/min. Pictures of the stones were taken before and after the test. When the test was finished one could obtain the force–displacement relationship for the stone. This procedure was repeated for the 15 stones in the test sample.

The stones were oriented in what was considered a likely orientation to get stuck in the switch. Note however that the stones in the test are all loaded vertically. In reality the loading condition of the stone would be horizontally where the train load will also add a significant contribution to the rail. Thus this test should overestimate the force required to crush a stone as compared to reality.

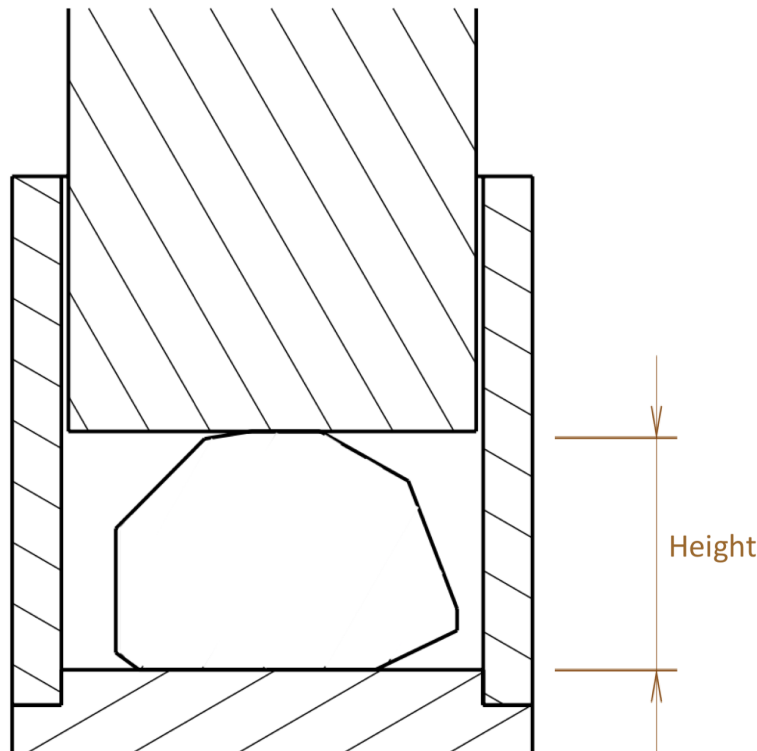


Figure 3.3: Illustration of the cross section of the hydraulic press test set up.

3.2 Estimation of maximum size of a ballast stone that may get trapped between switch and stock rail

This scenario concerns the trapping of a ballast stone. This occurs when the two switching motors close the tongue with a stone positioned between the switch rail and the stock rail. When switching is performed with a trapped stone, the switch rail will bend. It is assumed in this scenario that the stone will not fracture. This bending gives rise to reaction forces which the motors will need to overcome in order to properly perform the rail switching and lock the switch rail in place at the location of the motor. Figure 3.4 illustrates a trapped stone in a cross section view.

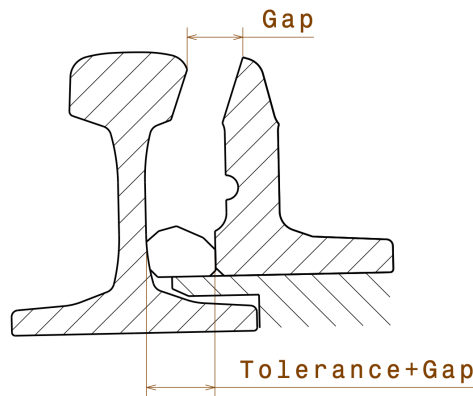


Figure 3.4: Stone stuck between switching rail and stock rail showing the distance created between the switch and stock rail.

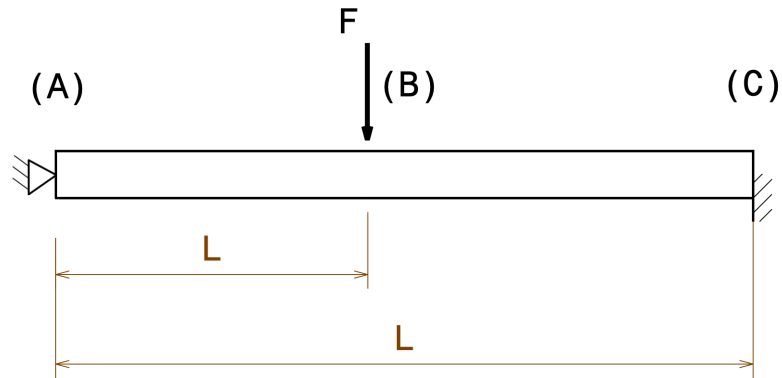
3.2.1 Numerical model of a switch rail

In Figure 3.5 and 3.6, a simplified model of the problem is presented. The boundary conditions are applied at (A) and (C) at the locations corresponding to the switch motors. At location (B) the load is applied. This location corresponds to that of the trapped stone.

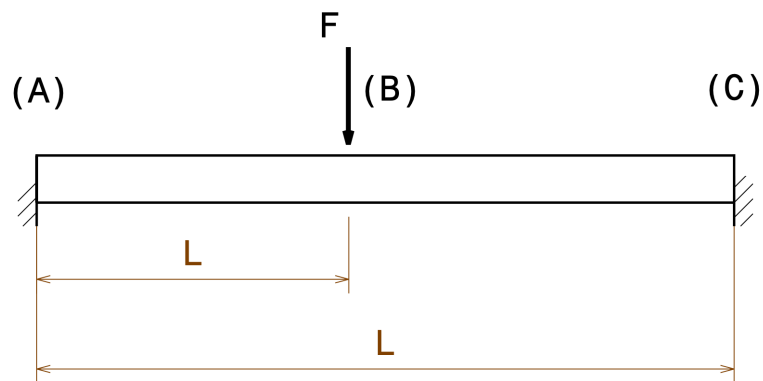
Some assumptions are introduced. In Figure 3.5 three different boundary conditions are presented. One is simply supported and one is partially clamped at both ends. The restricted displacement is applied at the foot of the rail for both cases. The last boundary condition is fully clamped at both ends. This boundary condition clamps the whole cross section at both ends of the rail. The surfaces at which the boundary conditions are applied are illustrated in Figure 3.6. Friction between the switch rail and the sliding plate during switching is neglected.

The trapped stone is assumed to be completely stuck and no sliding will occur. The sum of the forces generated by the switching motors will be applied where the stone is trapped at a distance L_F from (A). This will allow an evaluation of how

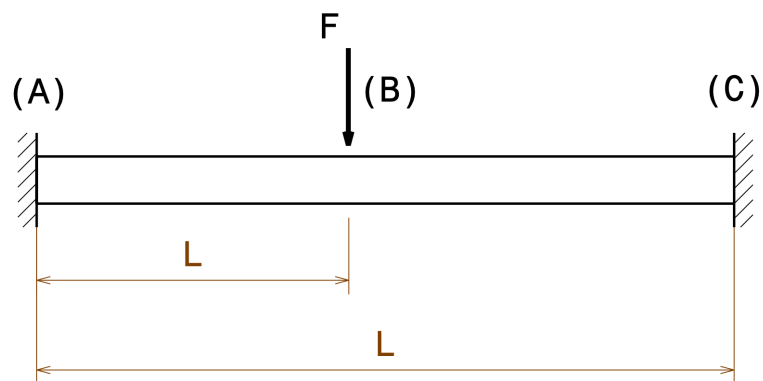
large deformation that is possible while the switch motors are still able to lock the switch rail at position (A) and (C).



(a) Simply supported – Partially clamped



(b) Partially clamped – Partially clamped



(c) Fully clamped – Fully Clamped

Figure 3.5: The three models of the switching rail. Switching motors are located at (A) and (C). The ballast stone is assumed to be stuck at (B). L is the total length between the switching motors and L_F is the length to the trapped ballast stone. The force F correspond to the sum of the forces generated by the switching motors.

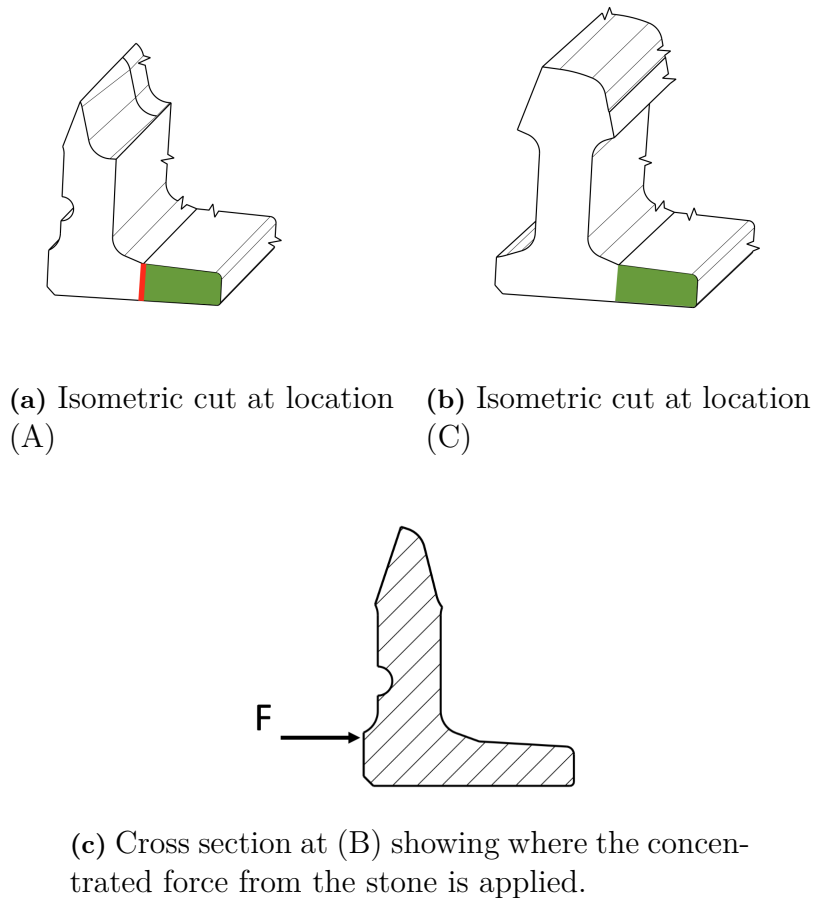


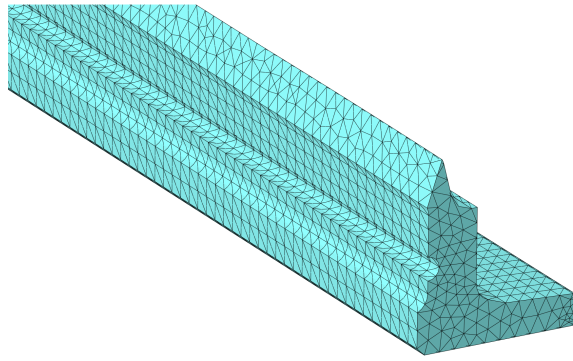
Figure 3.6: Cross sections for locations of interest on the switch rail. The red line correspond to where the simply supported boundary condition is applied. The green surface is where the partially clamped boundary conditions are applied. The fully clamped boundary conditions is applied to the whole cross section.

In order to find the location where the largest stone would get stuck, the influence of different distances L_F are investigated. The stone is assumed to only get stuck where there is a sliding plate. Reaction forces at locations (A) and (B) are evaluated to ensure that they do not exceed the maximum force that a switching motor could generate. If this is the case, the force F will be lowered so that the reaction forces are within possible magnitudes.

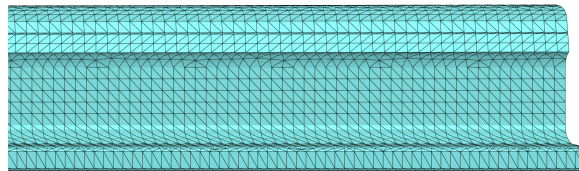
3.2.2 Finite element analysis of the switch rail

The geometry of the switching rail was provided by Vossloh Rail Services Scandinavia AB as a CAD model. This model was trimmed in order to only contain the section between the switching motors. The material of the rail was modeled as a linear elastic steel with a Young's modulus of 210 GPa and Poisson's ratio of 0.3.

The mesh was created in ABAQUS with quadratic tetrahedral elements of type C3D10. There was a total of 7977 elements, see Figure 3.7.



(a) Isometric view of the mesh at the rail end, location (A).



(b) Back view of the rail at location (C).

Figure 3.7: Part of the mesh of the switch rail. The mesh contains 7 977 elements. The elements are quadratic tetrahedron elements (C3D10).

Loads and boundary conditions were applied as indicated in Figure 3.5. The load was applied as a concentrated load with an initial magnitude of 13.6 kN. This load corresponds to the sum of the force the two switching motors can exert. Fully clamped boundary conditions were applied on the faces at the rail ends.

3.2.3 Validation of the switch rail finite element analysis

The finite element analysis was validated through comparison with an analytical model. This model was set up by assuming the switching rail behave as a common beam and solving it using Euler Bernoulli beam theory. One major difference from the finite element model is the simplification of the geometry. For the analytical problem the cross section was set as a constant L-beam shape. To validate the finite element model, displacement and reaction forces are compared towards the analytic solution given by the Euler–Bernoulli beam equation 3.1.

$$\frac{d^2}{dx^2} \left(EI \frac{d^2 w}{dx^2} \right) = q \quad (3.1)$$

The second moment of inertia, I , was taken as $5.4 \cdot 10^{-6} \text{ m}^4$ by estimations from the switch rail. Young's modulus was set to 210 GPa as for the FE model. The equation is integrated with regards to x in two parts. One from $x = 0$ to $x = L_F$ and the other from $x = L_F$ to $x = L$. The load and clamping are applied as boundary conditions.

3.3 Mechanical behaviour of trapped ballast stone

This model concerns the crushing of a stone that is stuck between the rails. The focus is to investigate stress and strain distribution in the loaded stone and whether or not the stone will break. The concept of how this problem is modeled is illustrated in Figure 3.8.

3.3.1 Model of ballast stone crushing

The model features a stone stuck between two steel plates. The loading of the stone is created by one of the plates being fixed while the other is loaded by a concentrated force, F , equal to that created by the switch motors as sketched in Figure 3.8.

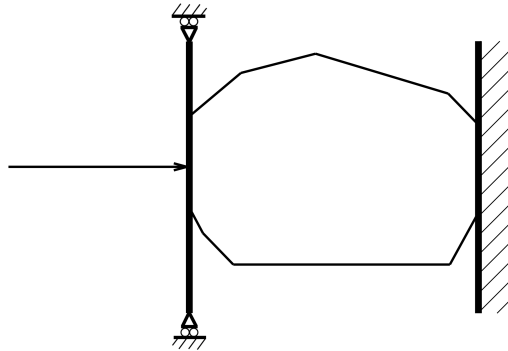


Figure 3.8: The model of a ballast stone between two rigid plates.

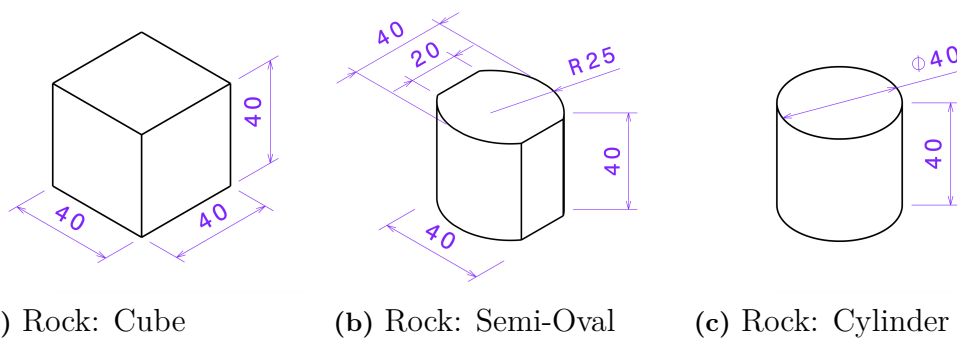
The stone is modeled as a solid homogeneous 3D body while the two plates are modeled as rigid bodies. The granite material is modeled with a linear Drucker–Prager model. The material parameters used are given in Table 3.2. The material parameters come from tests made on Bohus granite made by H. Shariati et. al [15]. The strain fracture limit used in the simulations is based on the strain limit of Solenhofen limestone [16].

3.3.2 Stone geometries

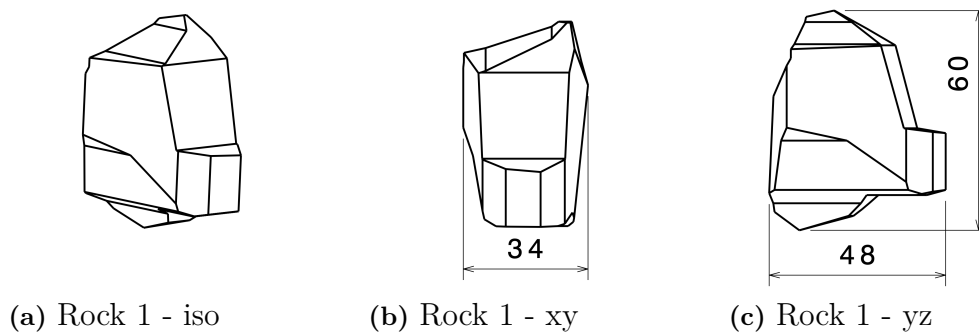
In total five different geometries were simulated. Three of them theoretically perfect geometries. One cube, one semi-oval and one cylinder. These can be seen in Figure 3.9. All stones are created to have length, width and height of 40 mm. The semi-oval rock will be loaded on the rectangular flat faces.

Table 3.2: Material parameters for granite used in the Drucker-Prager model

Density	ρ	2630 kg/m ³
Young's modulus	E	52 GPa
Poisson's ratio	ν	0.25
Friction angle	β	52°
Cohesion of material	d	153 MPa
Dilation angel	Ψ	40°
Strain fracture limit	ϵ_L	0.001

**Figure 3.9:** Isometric view of theoretical rock geometries with dimensions in mm.

Two shapes were modeled after real stones. One of the chosen stones was more cubic while the other had a more rounded shape. The geometries and some key dimensions can be seen in Figure 3.10 and Figure 3.11. These stones were both loaded in their shortest direction, i.e horizontally in the view in Figures 3.10b and 3.11b. Their real counterparts can be seen in the Appendix.

**Figure 3.10:** Real rock: Cubic

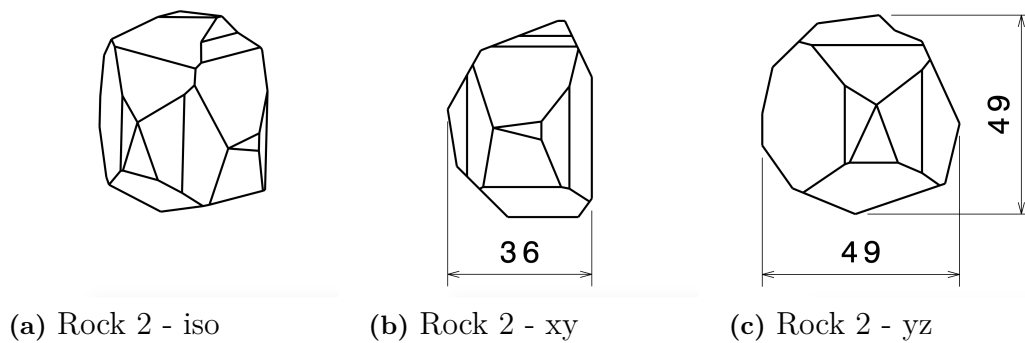


Figure 3.11: Real rock: Round

3.3.3 Setting up the finite element analysis

The problems were solved using ABAQUS Explicit. Symmetry was used for the theoretical models. This required only one-eighth of the geometry to be modelled and hence reduced computational times.

3.3.3.1 Overcoming numerical problems with large deformations

Some of the geometries will result in large deformations during loading. In order to circumvent potential numerical problems due to severely deformed elements, the NLGEOM option which accounts for non-linearities by introducing a nonlinear strain tensor is employed [17]. This setting is turned on by default in the ABAQUS Explicit [18].

An additional method that can be employed is the Arbitrary Lagrangian-Eulerian adaptive meshing. This will later be referred to simply as adaptive meshing. The adaptive meshing will both create a new mesh and will use advection to remap solution variables from the old mesh to the new [19].

The third major method used to prevent problems due to large deformations is to introduce smooth particle hydrodynamics (SPH). This options will transform elements that reaches a maximum principal strain to particles. These particles will be able to interact with the main FE simulation [20].

3.3.3.2 Meshing geometries

Some effort went in to creating good meshes in order to avoid numerical problems as well as trying to obtain a good resolution at stress concentrations. In Figure 3.12 the meshes for the theoretical stones can be seen. The mesh for the real stones can be seen in Figure 3.13. The number of elements for each model is provided in Table 3.3.

Table 3.3: Number of elements for the finite element models

Theoretical	Cube	8 000
	Oval	16 740
	Cylinder	15 880
Real	Cubic	8 100
	Round	8 221

As the geometries for the theoretical stones are simple, brick elements could be used. These elements were all 8 node linear elements with reduced integration points and with hourglass control. Hourglassing is when non-physical deformation of the element occurs. The phenomena originates from the fact that the finite element scheme evaluates the integrals assuming constant stress [21]. The elements used for the real geometries are 4 node linear tetrahedrons.

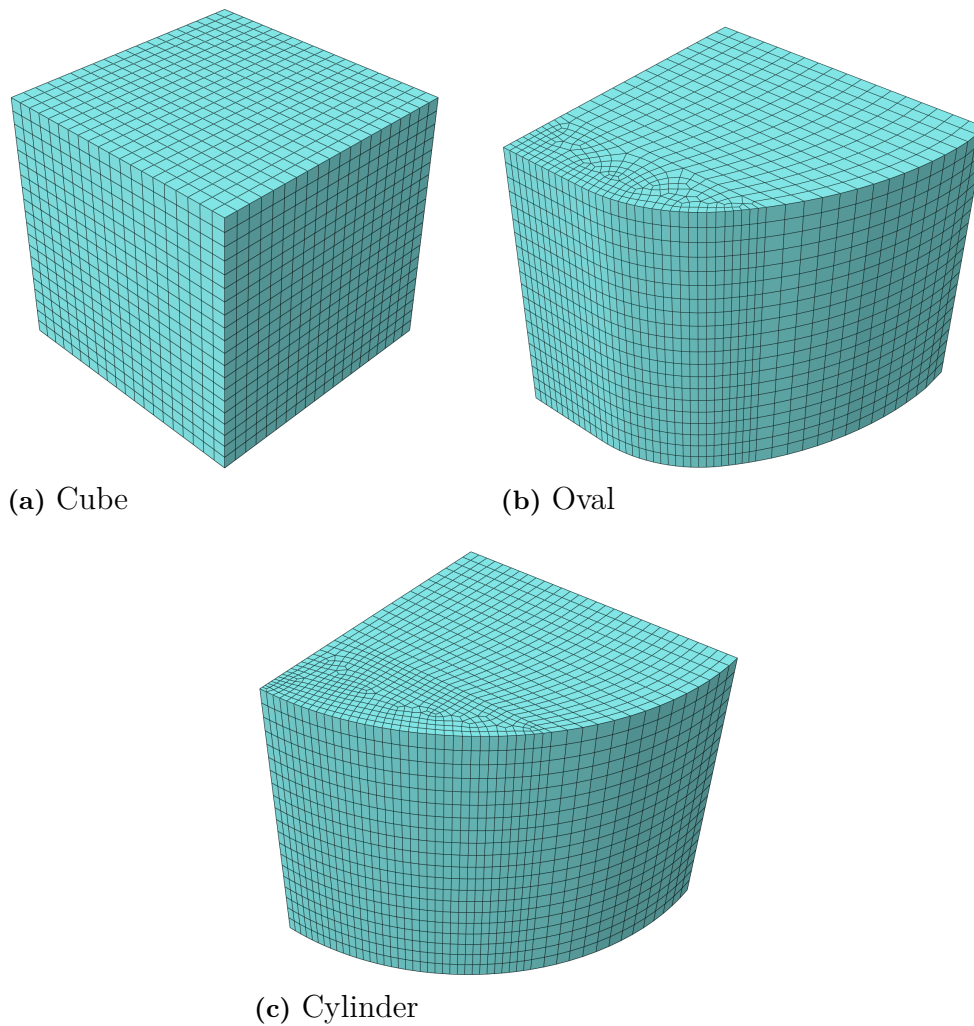
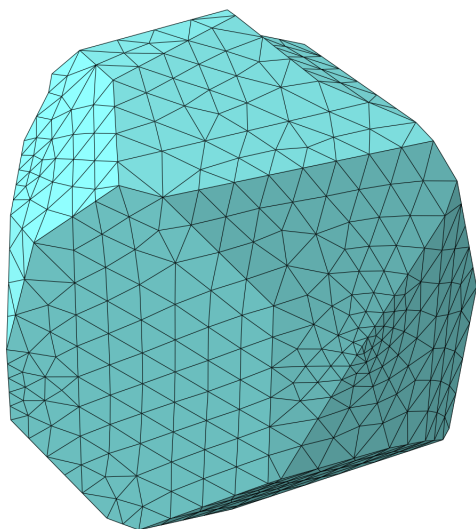
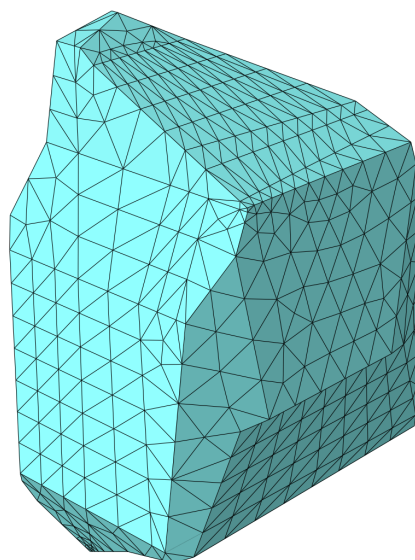


Figure 3.12: Mesh of the theoretical ballast stones. Note that only a quarter of the stones need to be meshed due to the use of symmetry.



(a) Round



(b) Cubic

Figure 3.13: Mesh of the real stones.

4

Results

4.1 Results of ballast stone crushing tests

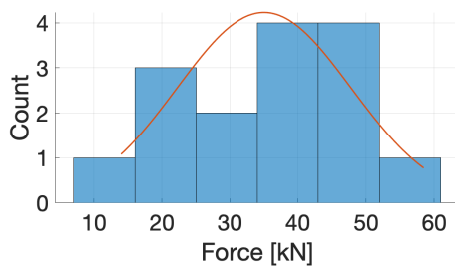
In the following section the results of the crushing tests are presented. In Table 4.1 the mass to height ratio and the maximum load for each stone is presented. A larger mass to height ratio would indicate bulkier stones.

In Figure 4.1 the distribution of maximum forces and force magnitude at the first load drop are presented. Here one may note that the maximum force follows a normal distribution but the force at the first load drop dose not. The average maximum force is 35 kN with a standard deviation of 13 kN. The median of the first load drop is 20 kN.

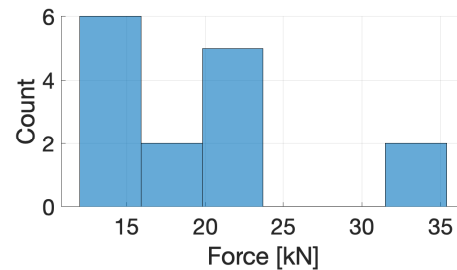
Table 4.1: The mass/height ratio (M/H) as well as the maximum load for each stone in the crushing test.

Stone no.	M/H	Max load [kN]
1	3.01	38.1
2	3.35	25.3
3	4.01	46.7
4	3.82	40.3
5	3.73	44.8
6	4.52	58.5
7	4.20	37.7
8	3.09	37.3

Stone no.	M/H	Max load [kN]
9	3.27	20.8
10	3.02	14.0
11	3.66	44.2
12	4.23	19.6
13	3.75	29.2
14	3.09	21.3
15	3.42	47.5



(a) Largest measured force.



(b) Force at first load drop in each test.

Figure 4.1: Distribution of maximum force and force magnitude at first load drop for the tested stones.

4. Results

In Figure 4.2a the force and displacement for the first load drop is presented. As the name indicates, a load drop is when there is a abrupt drop of the load magnitude, see Figure 4.3. This can be due to fracturing or sliding of the stone. The data shows only two instances where this force exceeds 25 kN. Due to insufficient amount of data it is impossible to conclude if these are outliers or regularly occurring data points. However all ballast stones experience the first load drop within a load range of 10 to 40 kN.

Figure 4.2 shows different force characteristics of the test data. The maximum force seems to have no correlation to the height of the specimen. However one may see some correlation between the maximum force and the mass of the stone.

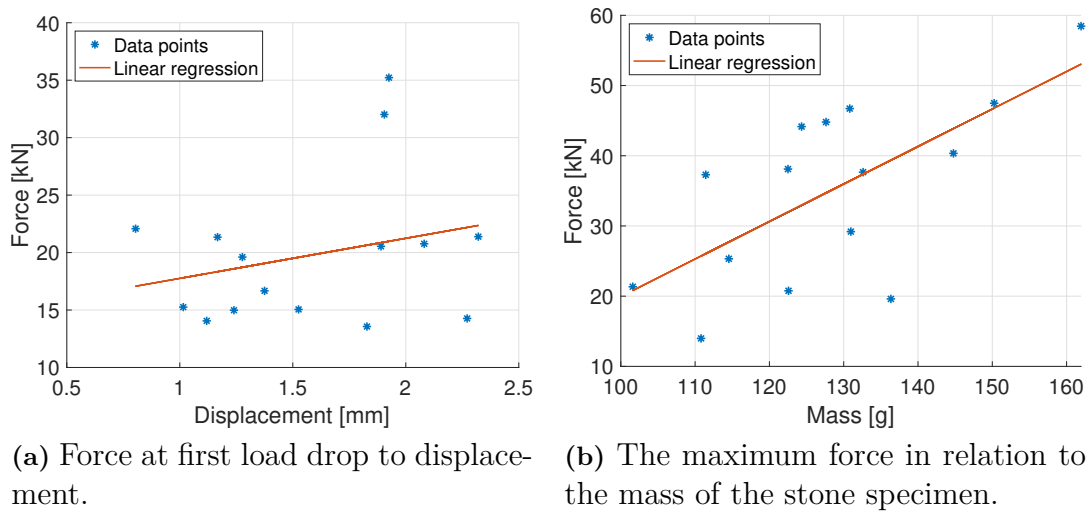


Figure 4.2: Force characteristics of the test data.

In Figure 4.3 the force–displacement curves can be seen for all tests made. The first real load drop is marked with a dashed line. The maximum force needed to crush a rock was 58 kN. The corresponding force–displacement curve is shown in Figure 4.3f.

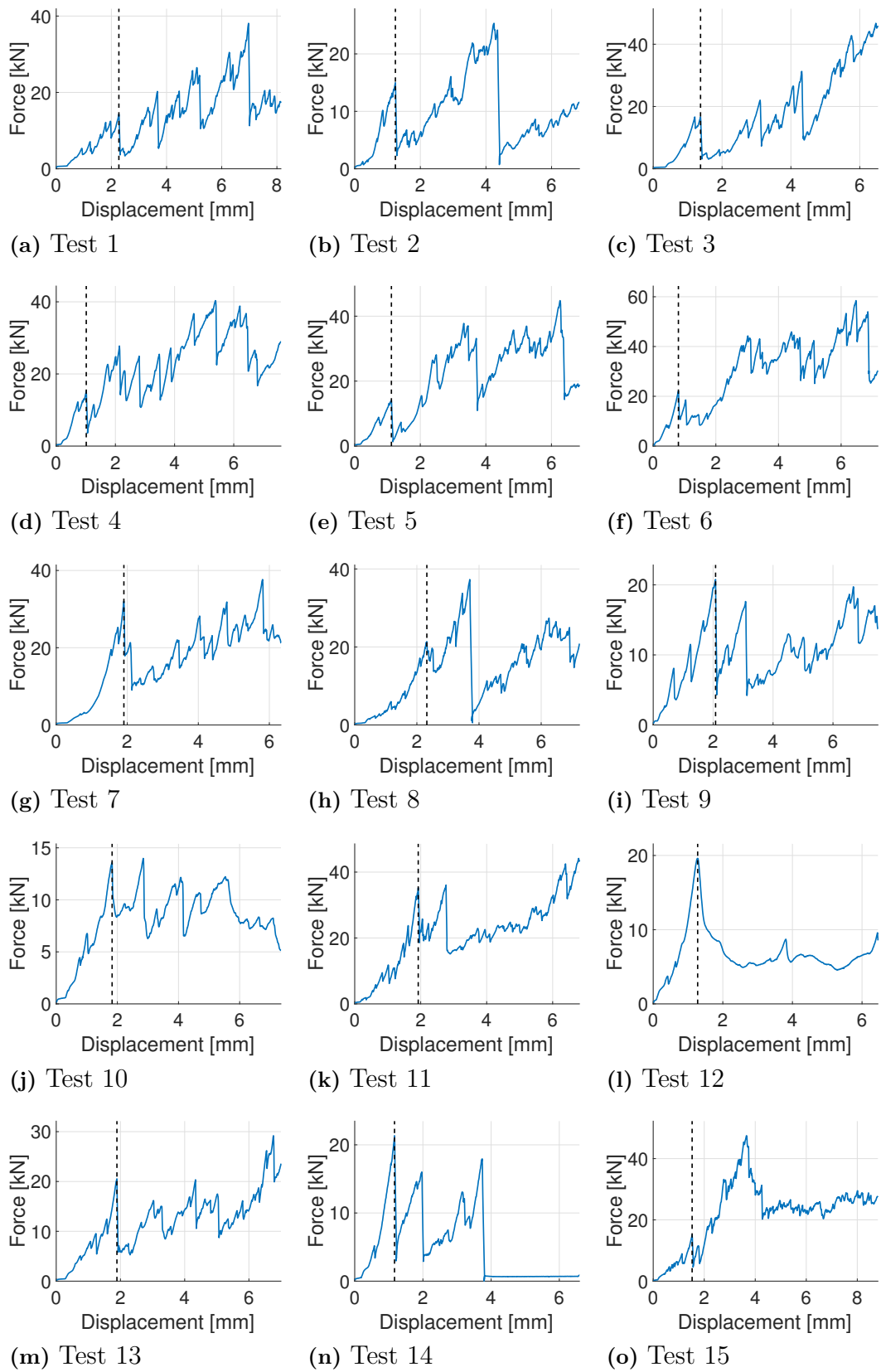


Figure 4.3: Force–displacement curves for the rock crushing tests. The first load drop is marked with a black dashed line.

4. Results

In Figure 4.3 there are some test results that should be noted. The stone in Test 14, Figure 4.3n, shatters and additional force is required to reach the 20 % compression limit. The stone in Test 12, Figure 4.3l has no real discrete force drop but shows more of a steady decline in load carrying abilities. The stone in Test 6, Figure 4.3f, is the one where the largest force is exerted during the 20 % compression of the test subject. Before and after pictures of these stones can be seen in Figure 4.4.



(a) Stone 6 - Before



(b) Stone 6 - After



(c) Stone 12 - Before



(d) Stone 12 - After



(e) Stone 12 - Splinter



(a) Stone 14 - Before

(b) Stone 14 - After

Figure 4.4: Before and after picture of some notable stones in the crushing test.

4.2 Results from finite element analyses

4.2.1 Bending of switch rail

The reaction forces and the largest displacements for the switch rail modelled with different boundary conditions are summarized in Table 4.2 and 4.3. In Table 4.2 the maximum horizontal displacement, maximum vertical displacement, the corresponding location and load are presented. The location is, as noted above, selected to always coincide with a sleeper position. Note that the load is adjusted so that the reaction force for a single motor does not exceed 6.8 kN. Reaction forces larger than this can not be exerted by the switch engine. The reaction forces and reaction moments are presented in Table 4.3.

In Figure 4.5 evaluated horizontal and vertical rail displacements are presented. As expected, the simply supported beam experiences the largest displacements. The fully clamped beam undergoes the least displacement.

Table 4.2: Maximum horizontal displacement, maximum vertical displacement, location where these occur, and corresponding adjusted load from the FE analysis of bending of switch rail.

Model	Location [mm]	Load [kN]	H. disp. [mm]	V. disp. [mm]
Simply supported	2447	12.92	81.05	31.79
Partially clamped	3647	13.60	50.35	17.57
Fully clamped	3647	13.50	42.45	13.03

Table 4.3: Reaction forces and moments from FE analysis of bending of switch rail.

Model	$R_{z,A}$ [kN]	$R_{z,C}$ [kN]	$M_{y,A}$ [kNm]	$M_{y,C}$ [kNm]
Simply supported	6.84	6.28	0	-13.52
Partially clamped	6.81	6.79	11.5	-12.30
Fully clamped	6.68	6.82	12.3	-13.68

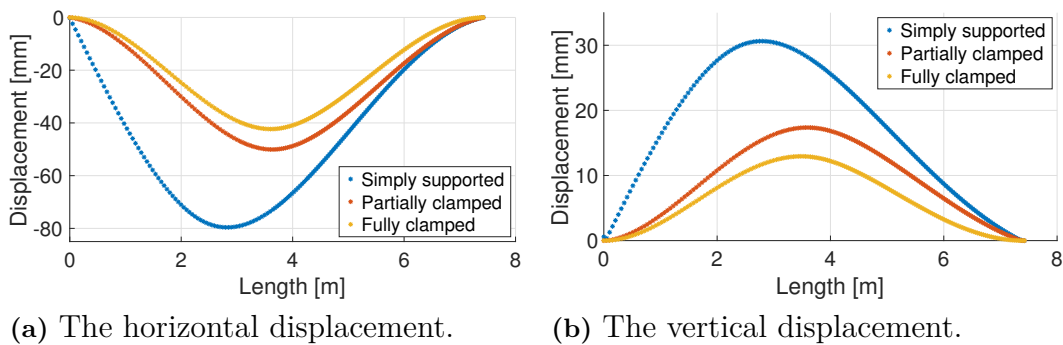


Figure 4.5: Displacement from FE analysis of bending of switch rail.

4.2.2 Uniaxially loaded ballast stones

In Figure 4.6 a comparison of force-displacement curves for the finite element simulations with and without smooth particle hydrodynamics (SPH) is presented. One may here note that the real "round" stone, as well as the theoretical cylinder stone show higher displacements than the rest of the stones. The round stone is loaded at a conical point while the cylindrical stone is loaded at a rounded surface. These are both areas where stress concentrations and large deformations will take place as they are geometrically weaker. The rest of the stones are all loaded on flat, broad surfaces. By comparing the simulation with SPH and without SPH one see larger compression for two of the simulations using the SPH criteria. These two are loaded at geometrically weaker points and thus the SPH criteria is triggered. For the rest of the simulations the strain limit is not reached. Thus the simulations are identical with those not employing the SPH criteria.

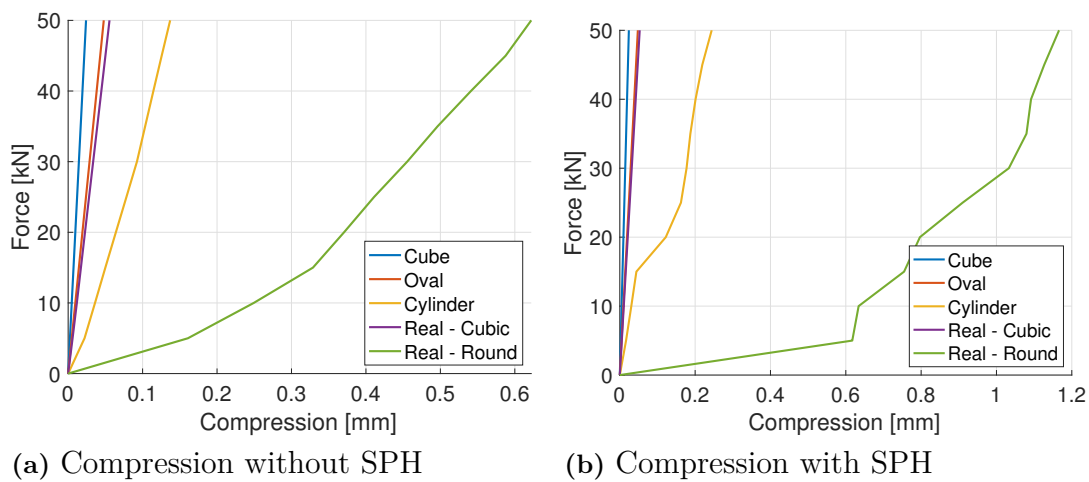
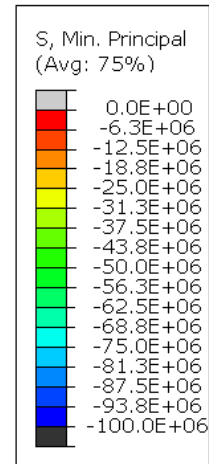
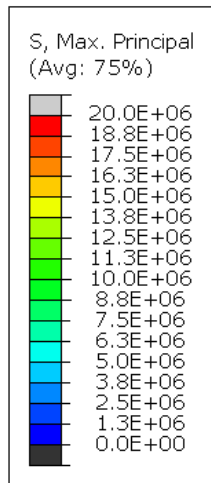


Figure 4.6: Comparison of the FE simulations of the deformation of compressed stones with and without SPH.

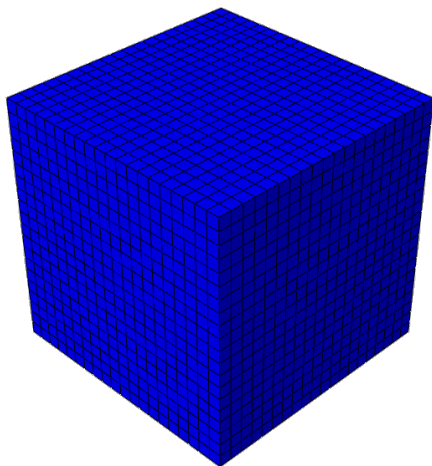
Figure 4.6 shows the maximum and minimum principal stresses for all stones at a load of 13.6 kN. Note that the cylindrical and the real round stone show the highest compressive principal stresses; both are above 100 MPa. The oval and the real cubic stones sustain compressive stresses at around 60 MPa with exceptions for a few small zones of stress concentrations. The cubic stone experience a compressive principal stresses of 8.5 MPa. Looking at the tensile principal stresses we see that once again the cylindrical and the real round stones presents the highest principal stresses close to and even above 20 MPa.

In comparison Siliceous granite has a compressive strength of 143 MPa and a tensile strength of 13.4 MPa [16]. If applied to the FE results, the the cylindrical and the real "round" stone would experience failure due to the high tensile stresses.

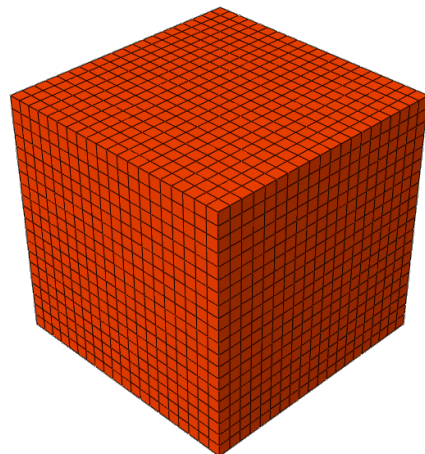


(a) Tensile principal stress scale [Pa] for the maximum principal stresses.

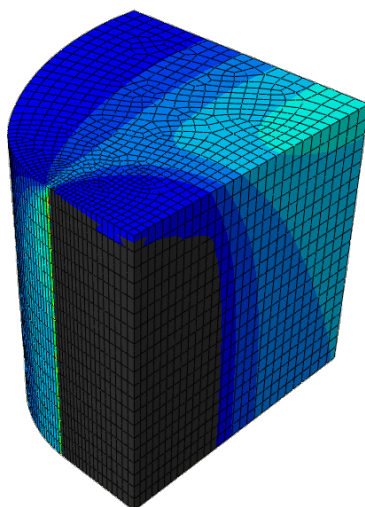
(b) Compressive principal stress scale [Pa] for the minimum principal stresses.



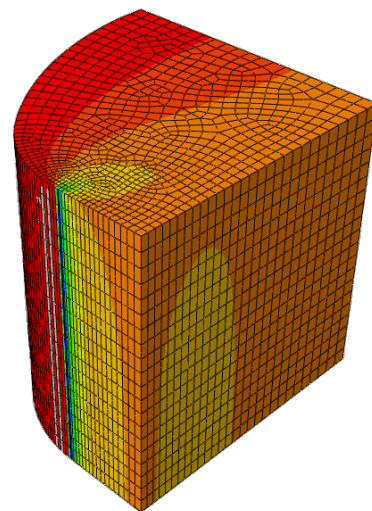
(c) Cube, tensile stress



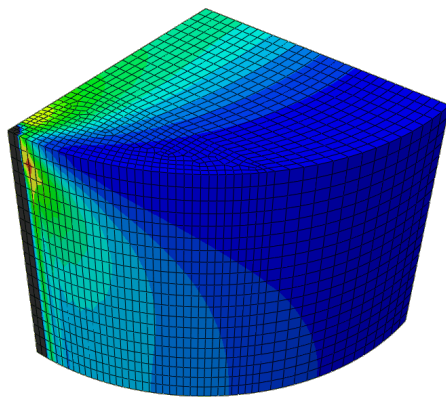
(d) Cube, compressive stress



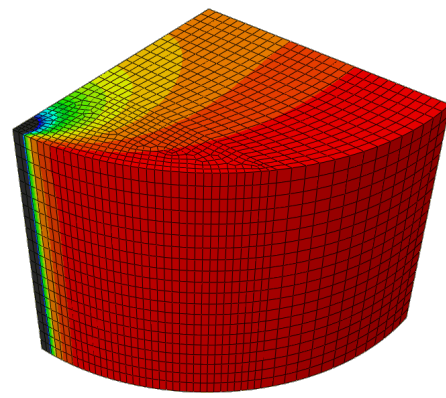
(e) Oval, tensile stress



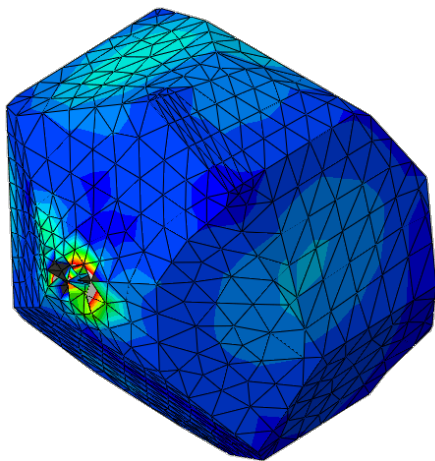
(f) Oval, compressive stress



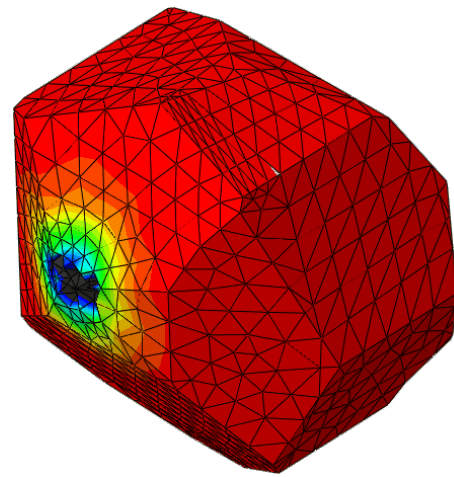
(g) Cylinder, tensile stress



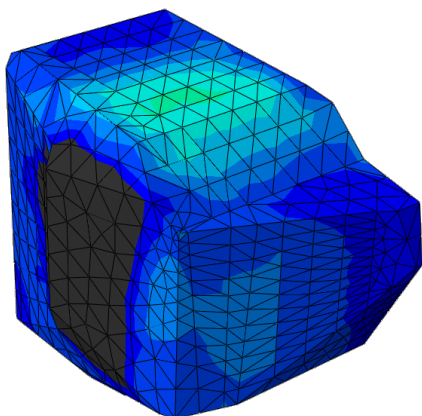
(h) Cylinder, compressive stress



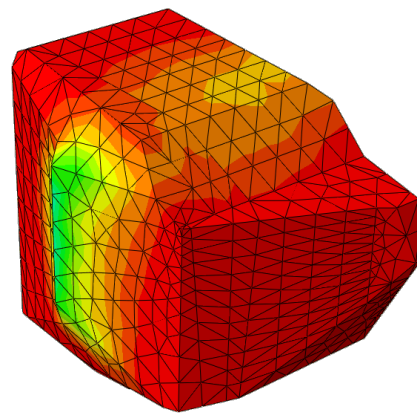
(i) Real round, tensile stress



(j) Real round, compressive stress



(k) Real cubic, tensile stress



(l) Real cubic, compressive stress

Figure 4.6: Maximum principal stresses at a load of 13.6 kN.

4. Results

In Figure 4.6 the equivalent plastic strain at the load 13.6 kN for the real round stone is presented. As can be seen, the plastic zone is located at the tip of the stone where the highest principal stresses occur. The real round stone is the only stone that undergo the Drucker–Prager plasticity. For all other stones the stresses are below the yield limit.

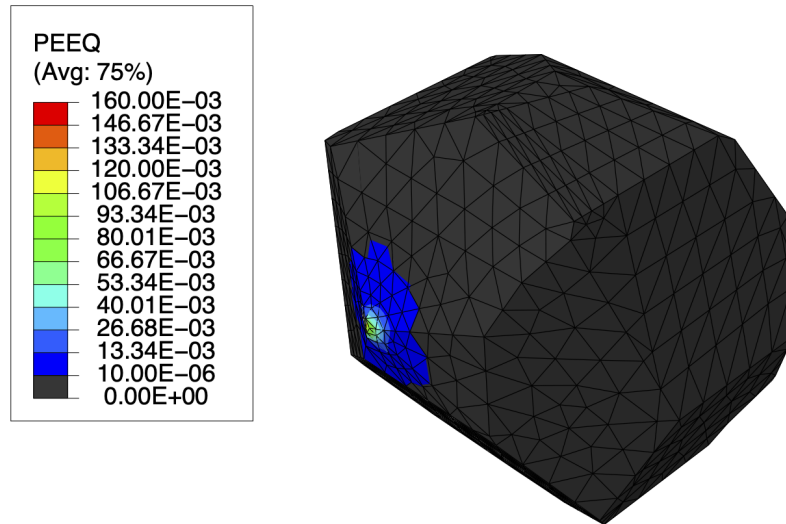


Figure 4.6: The equivalent plastic strain at a load of 13.6 kN for the real "round" stone.

4.3 Validations of finite element analyses

This section will investigate how valid the finite element simulations are compared to analytic and test data. The first subsection will compare how well the finite element model of the switch rail fits with an analytic Euler–Bernoulli beam solution. The second subsection will discuss how well the finite element model with the Drucker–Prager material model fits with test results.

4.3.1 Switch rail deformations

In Figure 4.7 below, the displacements evaluated by the finite element simulations and from the analytic Euler–Bernoulli beam equation are plotted. As can be seen, they do coincide quite well. However small discrepancies are to be expected as the cross section of the analytic model is constant while the rail model used in the finite element simulations has a varying cross section.

Note also that the analytical model does not account for three dimensional movement that includes also torsion. As seen in section 4.2.1 the rail will also rise from the ground. This might in reality move the stone and thereby change the point where the stone is loaded and thereby its load magnitude and the rail displacement. This is an important factor to consider in practise, but not included in the current study.

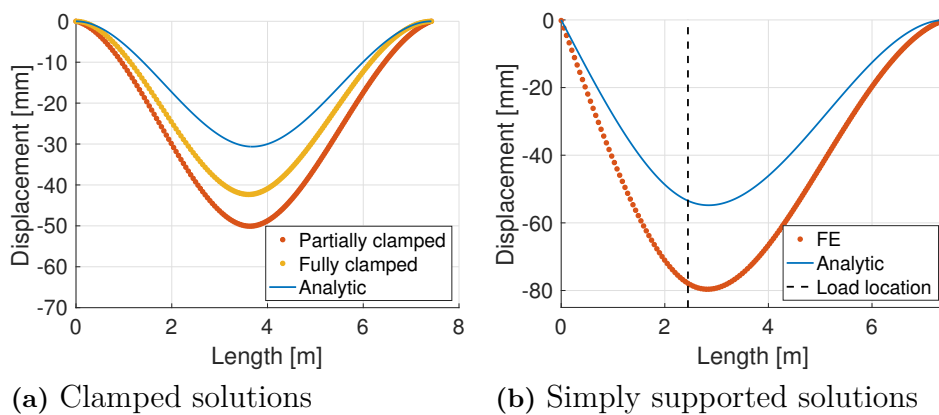


Figure 4.7: Displacement of the FE model compared with an analytic solution. Note that the analytic solution is fully clamped.

4.3.2 Stone crushing

As seen in Figure 4.8, test data and the modeled data do not fit well. The simulation result for the real round stones show the closest fit to test data, followed by the cylinder. The other stones are all off by a magnitude of 100.

The larger deformation in the cylinder and the real round stone is due to the smooth particle hydrodynamic, when applied, but also to their geometry. The cylinder has a rounded surface and the real round stone have a conical point where the load is applied. This gives rise to large deformations and in turn high strains. This explains the higher deformation seen in these models.

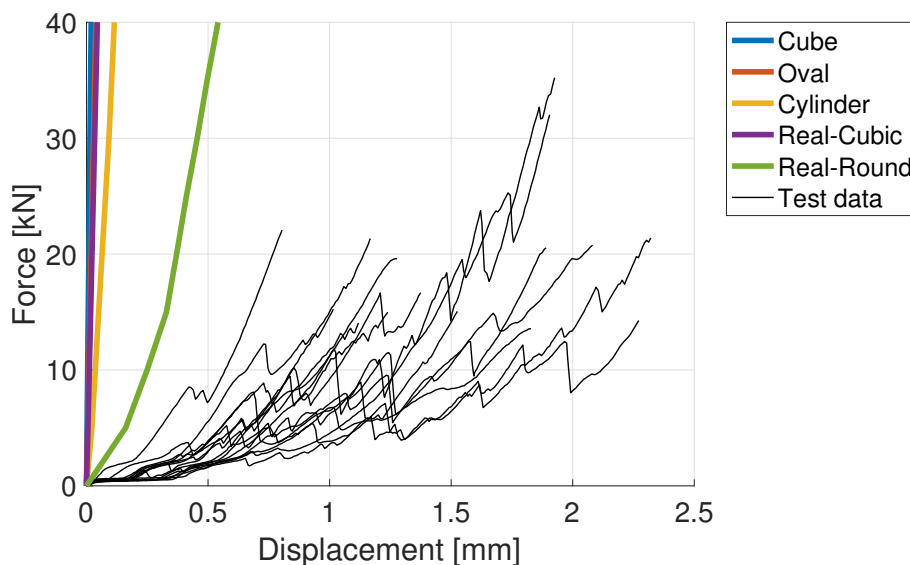


Figure 4.8: Displacement predicted by the FE models and evaluated from test data.

4.3.3 Comparing FE simulations of stone crushing to test data

Figure 4.9 shows a comparison of the real test data of two stones to those of the finite element simulations with and without smooth particle hydrodynamics. As seen in 4.9 and as discussed above, the fit in Figure 4.8 is not good.

In Figure 4.10 the distribution of the maximum principal stress obtained from the finite element simulations is compared to pictures of the fracture of the real stones are shown. The real stones have fractured in several places. For the round stone one may note that a fracture has occurred in a location where high stress concentrations are observed in the finite element analysis. For the cubic rock it is much harder to say what caused the fracture.

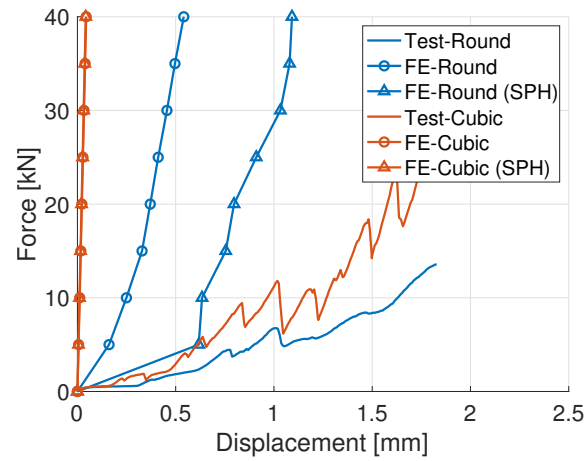
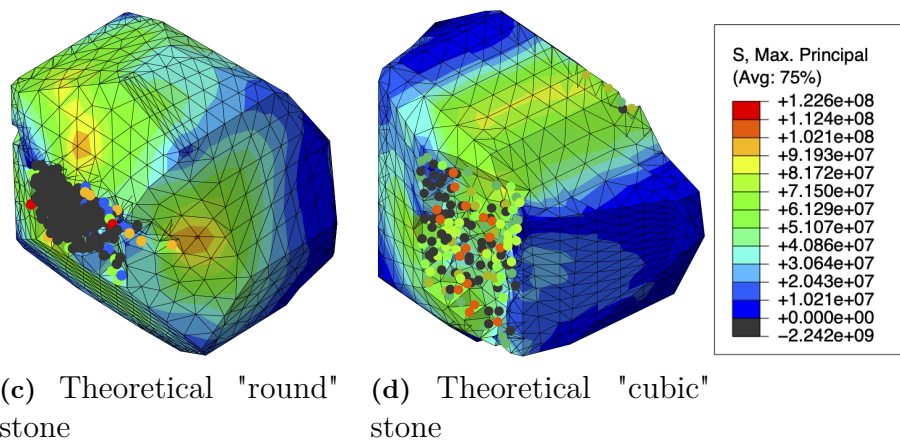


Figure 4.9: Comparison of displacement predicted in simulations and obtained from test data for the two stones.



(a) Crushed real round stone

(b) Crushed real cubic stone



(c) Theoretical "round" stone

(d) Theoretical "cubic" stone

Figure 4.10: Maximum principal stress in the finite element simulations stones and actual fracture surface of the tested stones. The round particles in the Figure (c) and (d) represent elements that have reached the imposed strain limit and been converted to free particles.

5

Discussion

5.1 Test data

The test data obtained were measured with precision and the validity of the data is good. However due to a relatively small sample size, the uniformity of the sample and the spread in results may be cause the test data to be insufficient to draw any final conclusion for how the ballast generally behaves.

However due to the uniformity of the particles tested one may still observe some interesting phenomena. The mean loading height was 35.6 mm with a standard deviation of 3.35 mm and a mean mass of 128.2 g with a standard deviation of 15.9 g. Both standard deviations are around 10 % of the mean value. By looking at the results we see that the mean maximum force to compress a stone 20 % was 35.0 kN. The corresponding standard deviation was 12.7 kN. This relates to 36 % of the mean maximum force.

Thus we can see that small deviation of stone properties, such as length and weight, can still give rise to a larger deviation in maximum load. The stones that required the largest force to reach the 20 % compression was the highest and second heaviest stone in the sample.

The test results show no clear correlation between the height of the stone and the required maximum load. This is shown in Figure 4.2. However some correlation is indicated between the mass of a stone and the maximum force. One can also draw the conclusion that a larger mass would mean a larger stone. Thus there should be a correlation between the size of the stone and the maximum load. It would however require further testing and larger sample sizes to determine this correlation with certainty.

5.2 Constitutive model

The constitutive model chosen was based on the linear Drucker–Prager model [15]. The model presented in [15] performed well in an indentation test. However as presented in Figure 4.8 the model does not predict the deformation of stones well. This could be due to the brittleness of granite and stones in general, as well as due to the different surface roughnesses of the stones. This would give rise to different local stress concentrations with macro and micro fractures as a result. In

order to get more accurate results this needs to be accounted for. One approach mentioned by H. Shariati et al. [22] is to introduce an anisotropic damage model that assumes initial material defects in the material. In addition, the progressive deformation after micro and macro fractures needs to be captured in the simulations.

Using smooth particle hydrodynamics, a given strain would detach the element to form a free particle. Studying the comparison between tests and the simulations of the two stones, Figure 4.9 shows how the smooth particle hydrodynamics (SPH) result in a fairly poor prediction of material detachment for the studied case. At a first glance it appears that simulations with the SPH criteria do in fact predict the displacement better than those without. However by looking at the actual fracture surface, Figure 4.10, it is clear that the SPH predictions do not show any resemblance to the actual fractures.

5.3 Simplifications and assumptions used in the switch blade deformation analysis

There are some significant assumptions made in this study to the scenario of a trapped ballast stone. One is the assumption of the ballast stone not moving along the rail when trapped. In Figure 4.7, one can see that the stone is not trapped in the position where largest deformation occurs. This introduces some interesting aspects not treated in this study. One is the non-uniaxial loading case. This refers to the fact that the stock rail and the switch rail are not tangential to one another. This type of loading would introduce a higher possibility of the stones sliding as well as different stress states of trapped stones.

Another scenario that was out of the scope of this study is the loading when a train passes. This scenario would require a dynamic simulation in order to properly capture the behavior of both the switch rail and the stone. A passing train would introduce new types of bending and torsion of the switch rail. This in turn would change the direction and magnitude of the loading.

Sliding of the stone is also something that might be interesting to study. As the wheel of the train approaches the trapped ballast stone, the stone would likely start to slide due to the direction of the loading. This sliding might release the stone.

Depending on the load created by a passing train it might also be of interest to consider the maximum lock force of the switch motors and check that the force normal to the rail are within this limit. A switch motor has a specified lock force of 100 kN with no specifications given for the axial force limit [7].

Another important aspect of the switch mechanics is how to model the boundary conditions at the switch rail actuators. As presented in Figure 4.5 there is almost a 40 mm difference between a fully clamped cross-section and a switch rail that is simply supported-clamped in the toe. The largest stone that could possibly get

stuck in a switch rail correspondsto a boundary condition with a simply support at one end. This stone could have a diameter of up to 81 mm. For a fully clamped cross section the largest stone that could get stuck would be a stone with the size of 42 mm. This would imply that there is a high possibility that stones smaller than 40 mm could get stuck and some possibility for stones smaller than 81 mm to get stuck, depending on the acting boundary conditions.

6

Conclusion

The aim of this study was to investigate the loading and deformation behaviour of trapped ballast stone in a railway switch. This have been done both with numerical analyses and physical tests. The following conclusions can be made with the result of the study as reference.

It can be concluded that ballast stones with a height of 40 mm requires loads in the range of 15 to 60 kN to reach a compression of some 20 %. There are also indications that the fracture load is affected by the weight of the stone. However there are no direct correlation between the loaded height of the stone and the fracture load.

The finite element analyses show that stones smaller than 42 mm could get trapped between the switch and the stock rail. The analysis also indicates that stones larger than 81 mm cannot get trapped with the switch rail in control. The study also demonstrates the difficulty in creating a numerical model of stone. As can be seen in the comparison between the numerical simulations and test results, a linear Drucker-Prager material model is not enough to capture the progressive damage of compressed granite.

7

Further work

There are some phenomena not touched upon in this thesis that require further investigations in order to assess the risk of derailment due to trapped ballast stones.

One topic which was outside the scope of this study was the dynamics of the switch and the stone. In order to make a proper assessment one would need to investigate the sliding of the stone due to the applied loads. Another subject is the dynamic loads due to passing trains. This would also deform the switch rail, which additional is an interesting aspect to further investigate. The loads and resulting rail deformation might push the stone so that it falls off the track, or the loads may simply be large enough to shatter the stone and thereby removing the risk of derailment. There is also the scenario of several stones getting trapped at the same time that would need further investigation.

Another topic that requires further study is the mechanics of the ballast stones. For numerical simulations to be reliable, the constitutive model of a ballast stone would need to be more sophisticated and take brittleness and progressive fracture into account. There is also a randomness in material properties of a ballast stone which require further analyses to fully establish.

Bibliography

- [1] Trafikverket, “Bandata.” <https://www.trafikverket.se/resa-och-trafik/Sveriges-jarnvagsnat/Bandata/>. Accessed: 2020-09-09.
- [2] J. Kristensson, “Växelfelen blir allt fler – Så ska de bekämpas. (Swedish),” *NyTeknik*, 2018-06-07.
- [3] U. Eriksson Charlotta, *Spårväxel Definition, benämning och förkortning*. Trafikverket, 2.0 ed., 2015.
- [4] F. Svedberg, “Spårväxelbyten längs den svenska järnvägen,” Master’s thesis, Luleå University of Technology, 2015.
- [5] L.-O. Karlsson, *Handbok Teknik: Del av metodik för inventering av järnvägens kulturmiljö*. KVM forum, 2015.
- [6] B. A. Pålsson, *Optimisation of Railway Switches and Crossings*. PhD thesis, Chalmers University of Technology, 2014.
- [7] S. FRITZ, *Teknisk specifikation: EasySwitch-R*. VOSSLOH COGIFER, 1 ed., 2014.
- [8] E.-L. Olsson, *KRAV: Banöverbyggnad Makadamballast*. Trafikverket, 0.3 ed., 2019.
- [9] S. S. Institute, *SS-EN 13450: Aggregates for railway ballast*. 1 ed., 2003-02-07.
- [10] *AMA: Anläggning 17*. Svensk Byggtjänst, 2017.
- [11] H. Jiang and Y. Xie, “A note on the Mohr–Coulomb and Drucker–Prager strength criteria,” *Mechanics Research Communications*, vol. 38, pp. 309–314, 2011.
- [12] Abaqus documentation MIT, “Extended drucker-prager models.” <https://abaqus-docs.mit.edu/2017/English/SIMACAEMATRefMap/simamat-c-druckerprager.htm>. Accessed: 2020-06-14.
- [13] L. Alejano and A. Bobet, “Drucker–Prager Criterion,” *Rock Mech Rock Eng*, vol. 45, pp. 995–999, 2012.
- [14] M. Ekh, *Mechanics of solids and fluids - Introduction to continuum mechanics*. 2017.
- [15] H. Shariati, M. Saadati, A. Bouterf, K. Weddfelt, P. Larsson, and F. Hild, “On the Inelastic Mechanical Behavior of Granite: Study Based on Quasi-oedometric and Indentation Tests,” *Rock Mechanics and Rock Engineering*, vol. 52, no. 3, pp. 645–657, 2019.
- [16] N. E. Dowling, *Mechanical Behavior of Materials - Engineering Methods for Deformation, Fracture, and fatigue*. Pearson Education Limited 2013, 4 ed., 2013.

- [17] G. Dhondt, “Calculix crunchix user’s manual version 2.7.” http://web.mit.edu/calculix_v2.7/CalculiX/ccx_2.7/doc/ccx/node245.html. Accessed: 2020-04-05.
- [18] Abaqus documentation MIT, “Accounting for geometric nonlinearity.” <https://abaqus-docs.mit.edu/2017/English/SIMACAECAERefMap/simacae-t-simstepmannlgeom.htm>. Accessed: 2020-04-05.
- [19] Abaqus documentation MIT, “Ale adaptive meshing and remapping in abaqus/explicit.” <https://abaqus-docs.mit.edu/2017/English/SIMACAEANLRefMap/simaanl-c-aleremesh.htm>. Accessed: 2020-04-05.
- [20] Abaqus documentation MIT, “Smoothed particle hydrodynamics.” <https://abaqus-docs.mit.edu/2017/English/SIMACAEANLRefMap/simaanl-c-sphanalysis.htm>. Accessed: 2020-04-05.
- [21] J. C. Schulz, “Finite element hourglassing control,” *International Journal for Numerical Methods in Engineering*, vol. 21, no. 6, pp. 1039–1048, 1985.
- [22] H. Shariati, M. Saadati, K. Weddfelt, P. Larsson, and F. Hild, “A damage model for granite subjected to quasi-static contact loading.” *Report TRITA-SCI-RAP 2019:006, 2019. Department of Solid Mechanics, KTH Engineering Sciences, Royal Institute of Technology, Stockholm, Sweden. To be submitted for international publication.*

Computational Resources

The computations were enabled by resources provided by the Swedish National Infrastructure for Computing (SNIC) at Chalmers University of Technology partially funded by the Swedish Research Council through grant agreement no. 2016-07213.

